Damping of relaxation oscillations,photon-photon resonance, and tolerance to external optical feedback of III-V/SiN hybrid lasers with dispersive narrow band mirror

Research Article | Vol. 30, No. 7 / 28 Mar 2022 / Optics Express 11090
Optics EXPRESS

Damping of relaxation oscillations, photon-photon resonance, and tolerance to external optical feedback of III-V/SiN hybrid lasers with a dispersive narrow band mirror

CRISTINA RIMOLDI,[1,*] LORENZO LUIGI COLUMBO,[1] JOCK BOVINGTON,[2] SEBASTIAN ROMERO-GARCÍA,[2] AND MARIANGELA GIOANNINI[1]

[1] *Dipartimento di Elettronica e Telecomunicazioni, Politecnico di Torino, Corso Duca degli Abruzzi 24, Torino, IT-10129, Italy*
[2] *Cisco Optical, Nuremberg, Germany*
[*] *cristina.rimoldi@polito.it*

Abstract: We address the stability of a tunable hybrid laser based on a III-V Reflective Semiconductor Optical Amplifier (RSOA) edge-coupled with a Silicon Photonic (SiPh) dispersive mirror through a model of time-delayed algebraic differential equations that accounts for the narrow band mirror. Our results allow to (i) analyze the stability of single mode lasing, (ii) quantify the impact of the mirror bandwidth on the damping of the laser relaxation oscillations and the emergence of photon-photon resonance, and (iii) study the tolerance of the laser to the external optical feedback. Thanks to this analysis, we find a mirror design that gives ultra-high stability up to an external feedback level of −10 dB. The aim of the work is providing a tool for understanding and interpreting the dynamics of these lasers and design configurations for isolator-free operation.

1. Introduction

Integration of laser sources in silicon photonics (SiPh) platform is still very challenging despite the many technological advancements that are now bringing the laser integration closer to commercial applications. Flip-chip bonding or heterogeneous integration of the III-V gain material in the silicon photonics process is now offered by some foundries in multi-wafer projects (see for example [1,2]) making possible the out-sourcing of silicon photonic integrated circuits including the laser part, which was almost missing until now [3]. Integrated laser sources are indeed not only essential for silicon photonics transmitters in optical communications (both datacom and telecom applications) but also in many other application fields such as sensing and LIDAR. In this context, the laser structure typically consists in a III-V gain material (flip-chip bonded [4] or heterogeneously integrated [5]) for light generation and amplification coupled to the rest of the silicon photonic chip, which provides also the mirrors to form the external laser cavity. Since the cavity mirrors can be designed in silicon photonics, there is a bunch of design solutions relying on various combinations of the passive components (i.e., micro-rings, DBR reflectors, Mach-Zehnder interferometers, delay lines, etc.). Thanks to this great design flexibility, lasers with long effective external cavities have been realized, supplying very narrow linewidth and wide tunability [6–9]. Interestingly, under proper bias currents and detunings of lasing wavelength, self-pulsing and self-mode locked regimes were also found [8,10].

Whereas the narrowing of the laser linewidth has been extensively studied both theoretically and experimentally [9,11], very few works have been dedicated to the analysis of other dynamic performances. The reflection coefficient of the silicon nitride mirrors with integrated high Q

#452155 https://doi.org/10.1364/OE.452155
Journal © 2022 Received 26 Dec 2021; revised 9 Feb 2022; accepted 28 Feb 2022; published 17 Mar 2022

Optics EXPRESS

micro-rings [12] can be a very narrow band filter with bandwidth spanning from a few GHz to sub-GHz as recently demonstrated in [13]. These mirrors can therefore exhibit an effective reflection coefficient that is highly dispersive in both amplitude and phase. This is very different from other integrated laser structures, based for example on DBR reflectors [14,15], the bandwidth of which is typically of the order of hundreds of GHz. However more recently low-kappa DBR reflectors in silicon nitride waveguides and with very narrow bandwidth were also demonstrated [16] indicating the high potential of the silicon photonics platform in the development of this kind of lasers.

The aim of this work is to theoretically investigate the impact of the dispersive narrow band reflector on the laser dynamic performance in presence of external feedback coming from the rest of the silicon photonics circuit or the output optical fiber. As an example, we investigate the laser structure detailed in Fig. 1, but the results and conclusions drawn here are more general and can be applied to any external cavity laser with dispersive narrow band reflector. The numerical method applied in our analysis is discussed in Section 2 and is based on the approach presented in [17] to study longitudinal mode competition in external cavity lasers composed by a Fabry-Perot laser and an external diffraction grating. In Section 3 we numerically study the impact, on the relative intensity and modulation bandwidth, of the silicon photonic mirror bandwidth, of the linewidth enhancement factor (indicated in the following as α factor), and of the detuning of the lasing mode with respect to reflectivity peak. The obtained results are in very good agreement with those obtained by performing a small signal analysis of the continuous wave solutions. In particular, we find that in some configurations relaxation oscillations are strongly damped and we expect that this can improve the tolerance of these lasers to unwanted external back reflections. On the other hand, the long effective cavity length of the hybrid laser is associated with the existence of a number of effective cavity longitudinal modes that may compete leading to continuous wave instability via photon-photon resonance (PPR). Despite in some cases PPR may be exploited to extended the direct modulation bandwidth of the laser, we may argue that it represents a detrimental factor for laser stability in presence of optical feedback. This scenario is confirmed by the results reported in Section 4, where we show that when relaxation oscillations are very damped thanks to the filtering effect of the mirror, the PPR becomes the main source of laser instability in presence of external feedback. Nonetheless, by estimating the critical feedback level (defined as the minimum external back reflection that makes the laser unstable) we demonstrate how dedicated designs of the dispersive mirror can guarantee an ultra-high tolerance to back reflections with lasers stable up to an external feedback level of −10 dB. This second part fits the framework of very recent research dedicated to the investigation of proper laser designs for isolator-free operation [15,18].

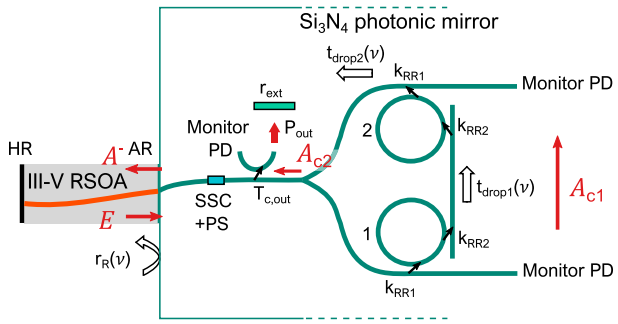

Fig. 1. Sketch of the considered hybrid laser structure. $t_{drop1}(\nu)$ and $t_{drop2}(\nu)$ are the trasmission spectra and monitor PDs are monitor photodiodes.

Optics EXPRESS

We observe that some results and considerations reported in this work are similar to those recently published in [19] for the photonic crystal Fano laser that was predicted to be very tolerant to the external optical feedback. However, we stress that the operation regime of the Fano laser is different with respect to the one of the III-V/SiN external cavity laser for two main reasons: (1) in Fano lasers the roundtrip of the electric field in the gain section is always much smaller than the photon lifetime in the external resonator (e.g., Fano resonator in [19]) and (2) only one longitudinal mode rules the laser dynamics because of the small effective length. It is therefore relevant to dedicate a study to silicon photonics external cavity lasers because, as we will demonstrate in this paper, their dynamic performance differs significantly from that of a Fabry-Perot or DBR laser and their tolerance to external optical feedback cannot be quantified by the standard Lang-Kobayashi approach.

2. Model

In this work, we consider hybrid lasers realized via the edge-coupling of a commercial III-V MQW HR/AR RSOA with silicon nitride (SiN) mirrors implemented on a silicon photonics platform according to the design in Fig. 1. Note that, while in the following we will often refer to the platform as a SiPh mirror, we use this terminology in its general sense and that in the present paper we consider only SiN waveguides. The laser front mirror in Fig. 1 is based on two coupled rings providing narrow band reflection and Vernier tuning, while the output power P_{out} is collected before the splitter using an output coupler. The ring radii ($R1$ and $R2$) are typically chosen ($\simeq$100 μm) to maximize the tuning range and minimize the overlap of the ring resonance peaks adjacent to the lasing one. Table 1 reports the parameters considered for the III-V RSOA of length L and the SiN photonic mirror. The power coupling coefficients related to the two microrings were chosen as $k_{RR1} = k_{RR2}$ (named k_{RR} later in the text) to provide maximum mirror reflection in the critical coupling regime. An analysis of the laser performance in terms of efficiency and tolerance to optical feedback of this and similar designs through a standard rate equation approach has been reported in [20], resulting in an optimized design with wall-plug efficiency (WPE) of about 18% at output power of 20 mW. In this study, it was demonstrated that, in comparison with other designs in the under-coupled regime ($k_{RR1}<k_{RR2}$), the configuration in Fig. 1 is overall more robust to perturbations induced by optical feedback. Moreover, the authors showed that this resilience increases with the effective length of the SiPh mirror.

In this paper, we extend the study of these devices, through the implementation of a more realistic model, which takes into account the frequency-selective effective reflectivity of the SiPh mirror. Here, we indicate with $r_{eff}(\omega)$ the frequency-dependent reflection coefficient at the right end side of the AR-coated facet of the RSOA due to the sole SiPh mirror. To account for possible external reflections due to spurious back reflections at the laser output, we add in our scheme an external reflector, with reflection coefficient r_{ext}, located at a distance L_{ext} from the output coupler (see Fig. 1). The total reflection coefficient due to both the SiPh mirror and the external optical feedback is thus indicated as $r_R(\omega)$ and read as:

$$r_R(\omega) = r_{eff}(\omega) + t_{SSC}^2 T_{c,out} r_{ext} e^{-i\phi_{ext}} e^{-i\tau_{ext}(\omega-\omega_0)} = |r_R(\omega)| e^{i\phi_R(\omega)} \tag{1}$$

where t_{SSC} is the spot size converter (SSC) transmission coefficient, $T_{c,out}$ is the output coupler power transmission coefficient, τ_{ext} is the external cavity delay, and $\phi_{ext} = 2L_{ext}\omega_0 n_{eff,SiN}/c$ with $n_{eff,SiN}$ effective refractive index in the SiN waveguide and ω_0 reference angular frequency.

The model is based on a set of time-delayed algebraic differential equations [17,21] in the reference plane at the AR-coated facet of the RSOA. The chosen approach considers an evolution equation for the slowly varying envelope of the electric field $E(t)$ (output of the SOA at the AR-coated facet and incident on the SiPh mirror), derived from the roundtrip equation in the frequency domain [17], which is expressed so that $|E|^2$ (in W) is the traveling power [17]. We indicate with $A_{c1}(t)$ the envelope of the electric field out of the drop port of ring 1 (see Fig. 1)

Optics EXPRESS

Table 1. Hybrid laser parameters

Definition	Symbol and Value
SOA parameters	
High reflection facet coefficient	$r_1^2 = R_1 = 0.9$
Internal quantum efficiency	$\eta_i = 0.76$
Length	$L = 0.1$ cm
Active region volume	$V = 1.5 \times 10^{-10}$ cm^3
Effective refractive index	$n_{eff} = 3.5$
Group refractive index	$n_g = 3.8$
Internal loss	$\alpha_i = 7.6$ cm^{-1}
Linewidth enhancement factor	$\alpha = 3$
Carrier lifetime	$\tau_N = 1$ ns
Transparency carrier density	2.1×10^{17} cm^{-3}
Modal gain coefficient	$g_N = 38$ cm^{-1}
Carrier reference wavelength	$\lambda_0 = 1.31\,\mu$m
SiPh mirror parameters	
SSC insertion loss	2 dB
Waveguide effective refractive index	$n_{eff,SiN} = 1.55$
Waveguide group refractive index	$n_{g,SiN} = 1.76$
Power output coupler coefficient	$T_{c,out} = 0.73$

and with $A_{c2}(t)$ the envelope of the electric field after propagation in ring 2 and the splitter. We assume that ring 1 and ring 2 are tuned to align both ring resonance wavelengths at ω_0. Under this hypothesis and assuming the time response of each ring to be Lorentzian [22] in the spectral range around ω_0, we get the following set of equations:

$$E(t) = \frac{e^{i(\omega_s-\omega_0)\tau_{in}} \exp\left(\frac{1}{\tau_{in}} \int_{t-\tau_{in}}^{t} L\left(1 + i\alpha\frac{\omega_s}{\omega_0}\right) g_N \ln\left(\frac{N(\bar{t})}{N_s}\right) d\bar{t}\right)}{r_R(\omega_s)} A^-(t-\tau_{in}) + F(t) \tag{2}$$

$$\frac{dA_{c1}(t)}{dt} = \gamma_{c1} t_{SSC} \sqrt{1 - T_{c,out}} E(t - \tau_{in,SiN}/2) e^{-i\Delta\phi/2} - \gamma_{t1} A_{c1}(t) \tag{3}$$

$$\frac{dA_{c2}(t)}{dt} = \gamma_{c2} A_{c1}(t) - \gamma_{t2} A_{c2}(t) \tag{4}$$

$$\frac{dN(t)}{dt} = \frac{\eta_i I}{qV} - \frac{N(t)}{\tau_N} - v_g g_N \ln\left(\frac{N(t)}{N_0}\right) \sigma \frac{|E(t)|^2}{V} \tag{5}$$

with

$$A^-(t-\tau_{in}) = t_{SSC}\sqrt{1 - T_{c,out}} e^{-i\Delta\phi/2} A_{c2}(t - \tau_{in} - \tau_{in,SiN}/2) + t_{SSC}^2 T_{c,out} r_{ext} e^{-i\phi_{ext}} E(t - \tau_{in} - \tau_{ext})$$

This set of equations assumes that the field circulates only in the counterclockwise direction, whereas in the real device it is split in two at the splitter. Our assumption is correct because the clockwise and counterclockwise light path are the same and we neglect the nonlinear response of the SiN rings and waveguides. In Eqs. (2–3), $\Delta\phi$ indicates a phase shift introduced by the phase control section (PS), which allows tuning of the lasing mode wavelength. In particular, we suppose that the value of $\Delta\phi$ derives from an additional phase section of length L_{ps}, whose variation

Optics EXPRESS

of effective refractive index Δn_{eff} can be tuned so that: $\Delta\phi = -4\pi\frac{\nu_0}{c}L_{ps}\Delta n_{eff}$. $\omega_0 = 2\pi c/\lambda_0$ in Eq. (2) is the reference angular frequency coincident with the resonance of the rings and ω_s is the angular frequency of the lasing mode at threshold carrier density N_s.

The first term on the right hand side of Eq. (2) accounts for the back-reflected field in the RSOA, whereas the second term $F(t)$ accounts for the spontaneous emission noise modeled as in [17]. α is the linewidth enhancement factor, g_N is the modal gain coefficient (including the optical confinement factor in the transverse plane). Equation (2) is coupled with the rate Eq. (5) for the spatially averaged carrier density $N(t)$ in the RSOA where η_i represents the internal quantum efficiency, q is the electron charge, v_g is the group velocity in the RSOA, V is the volume of the active region, N_0 is the carrier density value at transparency, and τ_N is the carrier lifetime in the RSOA. The RSOA parameters α, N_0, g_N are obtained through best fitting of the available experimental data [20]. We indicate with $\tau_{in,SiN}$ the time delay related to the path in the straight waveguide parts of the SiPh integrated circuit (i.e. SSC, phase section, splitter, etc.) and with τ_{in} the RSOA cavity roundtrip time. σ is a coefficient that accounts for the average of the electric field, such that $\sigma|E(t)|^2/V$ is the average photon density per unit volume in the RSOA. This parameter is dependent on the frequency ω_s and its value is assigned under the assumption that the relation between power and photon number derived for CW emission remains valid even in the CW unstable regime. More details on the expression of σ and model derivation are reported in the Supplementary materials and can be also found in [17,23].

Note that, if we approximate in Eq. (2) $E(t+\tau_{in}) \approx E(t) + \tau_{in}dE/dt$, assuming $\Delta\omega\tau_{in} \ll 1$ (where we defined $\Delta\omega = \omega - \omega_0$), we obtain a delayed differential equation for the electric field [24]; however, this would greatly limit the validity of the model to a range $\Delta\nu \ll 6$ GHz (for $\tau_{in} \approx 25$ ps corresponding to the RSOA length $L = 1$ mm and $\nu = \omega/2\pi$), thus making it impossible to extract any conclusion on the laser dynamics in a bandwidth larger than just a few GHz. Here, on the contrary, we want to adopt a more general approach with the goal of studying the laser dynamics for various bandwidth of the SiPh mirror reflection coefficients from a few GHz (e.g. 3 GHz) up to several GHz (e.g. 11 GHz or more).

The coefficients $\gamma_{c1,2}$, $\gamma_{t1,2}$ account respectively for the rate at which the electric field is coupled into the ring from the bus waveguide and the rate at which the electric field from the ring is lost, due to waveguide loss and coupling out to the bus waveguide. These coefficients can be calculated [22] as functions of the coupling coefficient k_{RR}, the ring losses $A_{loss1,2}$ and power coupling loss η:

$$\gamma_{c1,2} = \frac{v_{g1,2}k_{RR}(1-\eta)}{2\pi R_{1,2}t_{RR}A_{loss1,2}^{1/4}} \qquad \gamma_{t1,2} = \frac{v_{g1,2}\left(1 - t_{RR}A_{loss1,2}^{1/2}\right)}{2\pi R_{1,2}t_{RR}A_{loss1,2}^{1/2}}$$

where $v_{g1,2}$ are the group velocities inside the two rings and we defined $t_{RR} = 1 - k_{RR}(1-\eta)$. The effective reflection coefficient $r_{eff}(\omega)$ at the RSOA AR-coated plane due to the SiPh mirror, defined as the ratio $A^-(\Delta\omega)/E(\Delta\omega)$ when $r_{ext} = 0$, is therefore calculated as:

$$r_{eff}(\omega) = \frac{\gamma_{c1}\gamma_{c2}t_{SSC}^2(1-T_{c,out})}{(\gamma_{t1}+i\Delta\omega)(\gamma_{t2}+i\Delta\omega)}e^{-i\Delta\phi}e^{-i\Delta\omega\tau_{in,SiN}} \tag{6}$$

which has shown to be in very good agreement with the reflectivity curve obtained through the cascading of the transmission matrices of the various blocks of the SiPh mirror shown in Fig. 1. Graphs of the modulus square and phase of the complex reflectivity $r_{eff}(\nu)$ for different choices of $\gamma_{c1,2}$ and $\gamma_{t1,2}$, utilized in this study, are reported in Fig. 2. It is also convenient to introduce the SiPh mirror effective length L_{eff} calculated as:

$$L_{eff} = -\frac{v_{g,SiN}}{4\pi}\cdot\frac{\partial\phi_{eff}(\nu)}{\partial\nu}\bigg|_{\nu=\nu_0} \tag{7}$$

Optics EXPRESS

where $\phi_{eff}(\nu)$ is the phase of the complex reflectivity $r_{eff}(\nu)$ and $v_{g,SiN}$ the group velocity in the SiN waveguide. The effective length L_{eff} accounts not only for the effective length of the rings, but also for the length of the arms between the splitter and the rings, the length of the straight waveguide coupling the two rings, and the length of the straight waveguide between the SSC and the splitter. In the results presented in this work, these are approximately 500 μm, 300 μm and 1 mm respectively, with their specific values dependent on the ring radii optimization. Since propagation loss in the straight SiN waveguides is assumed small in comparison with the SSC insertion loss, we have neglected optical loss in the waveguide sections mentioned above. Further, given the value of the ring radii, we also assume the bent waveguide losses to be negligible.

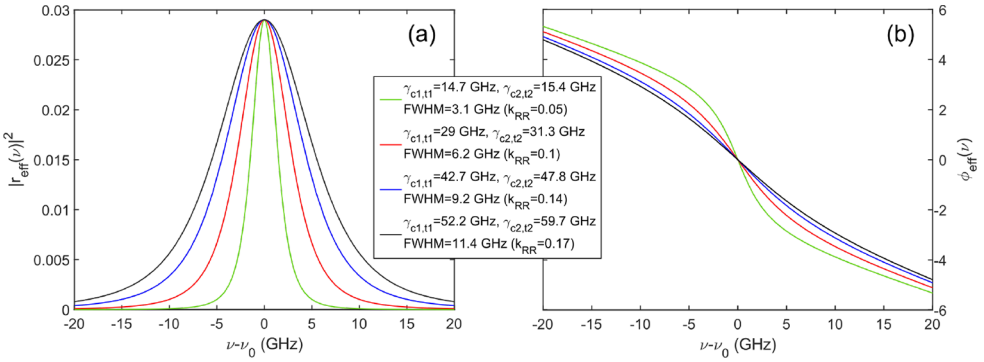

Fig. 2. Effective reflectivities in modulus square (a) and phase (b) as functions of frequency for 4 different choices of $\gamma_{c1,2}$, $\gamma_{t1,2}$ corresponding to the FWHMs of the $|r_{eff}(\nu)|^2$ indicated in the legend and considered in this study. In parenthesis we also report the corresponding value of k_{RR} in the ideal case of $\eta = 0$ and negligible losses for the bent waveguides.

2.1. CW longitudinal modes of the hybrid laser

The oscillation condition in the frequency domain reads [25]:

$$r_R(\omega) r_L(\omega, N) = 1 \tag{8}$$

with

$$r_L(\omega, N) = r_1 e^{-2iLk(\omega,N)} \tag{9}$$

and $r_R(\omega)$ as in Eq. (1). $k(\omega, N)$ is the wave vector

$$k(\omega, N) = \frac{\omega}{c} n_{eff}(\omega, N) + \frac{i}{2}\left[g(\omega, N) - \alpha_i\right]$$

with

$$n_{eff}(\omega, N) = n_{eff}(\omega) + n_{eff}(N) = n_{eff}(\omega) - \frac{\alpha g_N c}{2\omega_0} \log\left(\frac{N}{N_0}\right)$$

being the effective refractive index and $g(\omega, N) = g_N \ln(N/N_0)$ the modal gain in the RSOA. Solving the oscillation condition for modulus and phase, we obtain the following solutions for the steady (CW) states

$$N_s = N_0 \exp\left\{\frac{-\ln\left[r_1 |r_R(\omega_s)|\right] + \alpha_i L}{g_N L}\right\} \tag{10}$$

$$\Delta\omega_s = \omega_s - \omega_0 = \frac{1}{\tau_{in}}\left\{\phi_R(\omega_s) + \alpha\left[-\ln\left[r_1 |r_R(\omega_s)|\right] + \alpha_i L\right] + 2m\pi\right\} \tag{11}$$

with $\phi_R(\omega)$ defined in Eq. (1). As evident in Eq. (11), several CW longitudinal modes with pulsation ω_s associated with different values of m are solutions of the oscillation condition,

Optics EXPRESS

corresponding to different values of threshold carrier densities (as shown e.g. in Fig. 3(a,b) for the smallest and largest values of FWHMs of the $|r_{eff}(\nu)|^2$ considered in this study). The lasing mode is the one with the minimal N_s. However, as an effect of nonlinear wave mixing and phase-amplitude coupling provided by the α-factor, far from threshold the device can also lase on one of the other modes (mode hopping), solutions of Eqs. (10–11), or enter a multi-mode regime [17]. We can observe in Eq. (11) that for $\alpha \neq 0$ the carrier-dependent refractive index introduces a dependence of the longitudinal modes from the effective losses (including both internal loss and mirror loss $\alpha_m = -\ln(r_1|r_R(\omega_s)|)/L$). Further, the linewidth enhancement factor is responsible for the overall asymmetry of the CW mode positions (see also Fig. 3), which often causes less modes for $\Delta\nu>0$. In absence of back reflection from the passive parts of the SiPh circuit, we have $r_R(\omega) = r_{eff}(\omega)$ and we can clearly see that the phase shift $\Delta\phi$ (contained in the phase term $\phi_R(\omega)$) permits the tuning of the lasing mode with respect to the effective reflectivity peak at ω_0.

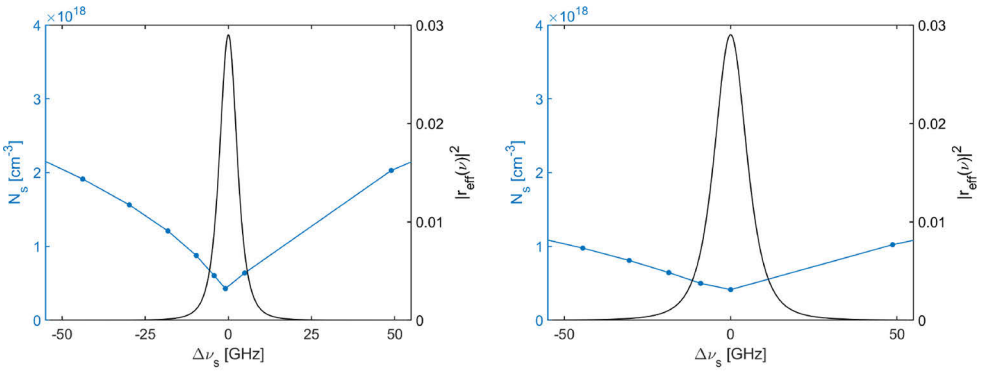

Fig. 3. (Left y-axis) Plot of the stationary carrier densities N_s (blue dots) as functions of the longitudinal mode frequency $\Delta\nu_s$, in absence of external optical feedback, computed according to Eqs. (10–11) for FWHM=3.1 GHz (a) and FWHM=11.4 GHz (b) for the $|r_{eff}(\nu)|^2$. (Right y-axis) Modulus square of the effective reflectivity for FWHM=3.1 GHz (a) and FWHM=11.4 GHz (b).

2.2. Small signal analysis

In order to gather information on the laser stability, we performed a small signal analysis (SSA) in the frequency domain [17] around the CW solutions. Here, we consider small perturbations of the steady states of the following form

$$E(t) = e^{i(\omega_s-\omega_0)t}[E_s + \delta E(t)] \tag{12}$$

$$A^-(t) = e^{i(\omega_s-\omega_0)t}[A_s^- + \delta A^-(t)] \tag{13}$$

$$N(t) = N_s + \delta N(t) \tag{14}$$

This corresponds, in the frequency domain, to

$$\begin{aligned} E(\Delta\omega) &= E_s 2\pi\delta(\tilde{\omega}) + \delta E(\tilde{\omega}) \\ A^-(\Delta\omega) &= A_s^- 2\pi\delta(\tilde{\omega}) + \delta A^-(\tilde{\omega}) \\ N(\tilde{\omega}) &= N_s 2\pi\delta(\tilde{\omega}) + \delta N(\tilde{\omega}) \end{aligned}$$

where $\tilde{\omega} = \omega - \omega_s$, $A_s^- = r_R(\omega_s)E_s$, and $\delta A^-(\tilde{\omega}) = r_R(\omega)\delta E(\tilde{\omega})$ already accounts for the perturbation in the variables A_{c1} and A_{c2}. Note also that the perturbed steady state of $A^-(\Delta\omega)$

Optics EXPRESS

includes the effect of the external feedback. Each perturbation can be expanded on the Fourier basis

$$\delta E(t) = \frac{1}{2\pi}\int_{-\infty}^{+\infty} \delta E(\tilde{\omega}) e^{i\tilde{\omega}t} d\tilde{\omega} \tag{15}$$

Substituting Eqs. (12–14) in Eqs. (2) and (5), the resulting perturbation equations in the Fourier domain are

$$\delta N(\tilde{\omega}) = -\frac{v_g g_N \sigma E_s}{V} \ln\left(\frac{N_s}{N_0}\right) \frac{\delta E^*(-\tilde{\omega}) + \delta E(\tilde{\omega})}{i\tilde{\omega} + \Gamma_N} \tag{16}$$

$$\begin{aligned}\delta E(\tilde{\omega}) =& \frac{r_R(\omega_s + \tilde{\omega})}{r_R(\omega_s)} \delta E(\tilde{\omega}) e^{-i\tilde{\omega}\tau_{in}} + E_s \frac{L g_N}{N_s \tau_{in}} \left(1 + i\alpha \frac{\omega_s}{\omega_0}\right) \frac{1 - e^{-i\tilde{\omega}\tau_{in}}}{i\tilde{\omega}} \delta N(\tilde{\omega}) \\ &+ \mathcal{F}(\omega_s + \tilde{\omega})\end{aligned} \tag{17}$$

where the spontaneous noise term has been expanded as follows [23]

$$F(t) e^{i\omega_0 t} = \frac{1}{2\pi}\int_{-\infty}^{+\infty} \mathcal{F}(\omega) e^{i\omega t} d\omega$$

and

$$\Gamma_N = \frac{1}{\tau_N} + \frac{v_g g_N \sigma}{V N_s} E_s^2$$

is the carrier density damping rate in a single-mode laser with frequency-independent reflection coefficient equal to $r_{eff}(\omega_s)$. This is the damping factor predicted by standard rate equations as in [26]. Note that in Eq. (17), the exponential in Eq. (2) as well as its logarithmic term have been linearized in the hypothesis that $\delta N(t - \tau_{in})/N_s \ll 1$ and we used the following equivalence

$$\int_{t-\tau_{in}}^{t} \delta N(\bar{t}) d\bar{t} = \frac{1}{2\pi}\int_{-\infty}^{+\infty} \frac{1 - e^{-i\tilde{\omega}\tau_{in}}}{i\tilde{\omega}} e^{i\tilde{\omega}t} \delta N(\tilde{\omega}) d\tilde{\omega}$$

Substituting Eq. (16) in Eq. (17), we therefore obtain the following expression [17,25]

$$[1 - G(\tilde{\omega}) + B(\tilde{\omega})]\delta E(\tilde{\omega}) + B(\tilde{\omega})\delta E^*(-\tilde{\omega}) = \mathcal{F}(\omega_s + \tilde{\omega}) \tag{18}$$

with

$$G(\tilde{\omega}) = \frac{r_R(\omega_s + \tilde{\omega})}{r_R(\omega_s)} e^{-i\tilde{\omega}\tau_{in}} \quad B(\tilde{\omega}) = \frac{1 - e^{-i\tilde{\omega}\tau_{in}}}{2i\tilde{\omega}} \frac{\omega_r^2}{i\tilde{\omega} + \Gamma_N} \left(1 + i\alpha \frac{\omega_s}{\omega_0}\right)$$

and

$$\omega_r^2 = \frac{v_g g_N \gamma \sigma |E_s|^2}{V N_s}$$

with $\gamma = v_g g_N \ln(N_s/N_0)$. As for Γ_N, the angular frequency ω_r is the relaxation oscillation frequency obtained assuming a frequency-independent effective reflectivity equal to $r_{eff}(\omega_s)$. As we will show in Section 3, the frequency and damping of the hybrid laser relaxation oscillations are also dependent on the effective length of the SiPh mirror, on the bandwidth of the narrow band reflector and on the α-parameter.

Equation (18) and its complex conjugate (where $\tilde{\omega}$ is substituted by $-\tilde{\omega}$ in order to refer to the same frequency) form a linear system of algebraic equations in the variables $\delta E(\tilde{\omega})$ and $\delta E^*(-\tilde{\omega})$. Here, the zeros of the system determinant correspond to the perturbation oscillations around the CW solution [26]. The determinant is given by:

$$D(\tilde{\omega}) = [1 - G(\tilde{\omega}) + B(\tilde{\omega})][1 - G^*(-\tilde{\omega}) + B^*(-\tilde{\omega})] - B(\tilde{\omega})B^*(-\tilde{\omega}) \tag{19}$$

According to our notation, the imaginary parts of the complex values of $\tilde{\omega}$, solving the equation $D(\tilde{\omega}) = 0$, are associated to the perturbation growth rate, while their real parts are associated to the

Optics EXPRESS

perturbation frequency. Thus, if the imaginary part of any $\tilde{\omega}$ is negative than the corresponding CW solution, defined by a specific value of (ω_s, N_s), is unstable.

Note that, for $r_{ext} = 0$, in the case of a single-mode laser with frequency-independent reflectivity (i.e. $r_R(\omega_s + \tilde{\omega}) = r_{eff}(\omega_s)$) and $\alpha = 0$ [26], the following approximations come into place

$$G(\tilde{\omega}) \approx 1 - i\tilde{\omega}\tau_{in} \tag{20}$$

$$B(\tilde{\omega}) \approx \frac{\tau_{in}\omega_r^2}{2(i\tilde{\omega} + \Gamma_N)} \tag{21}$$

and solving $D(\tilde{\omega}) = 0$ equals finding the values of $\tilde{\omega}$ solutions of

$$-\tilde{\omega}^2 + i\tilde{\omega}\Gamma_N + \omega_r^2 = 0\,. \tag{22}$$

Equation (22) is indeed the determinant of the standard rate equation system as in textbooks [26]. We define this case as the Fabry-Perot case. On the other hand, if we approximate the hybrid laser with a single-mode external-cavity laser with $\alpha = 0$, effective length L_{eff}, and reflection coefficient $r_{eff}(\omega) = |r_{eff}(\omega_s)|$ then

$$G(\tilde{\omega}) \approx 1 - i\tilde{\omega}\tau_{tot}$$

with $\tau_{tot} = \tau_{in} + \tau_{eff}$ and $\tau_{eff} = \tau_{in,SiN} + \gamma_{t1}/(\gamma_{t1}^2 + \Delta\omega_s^2) + \gamma_{t2}/(\gamma_{t2}^2 + \Delta\omega_s^2)$ being the full time delay of the external cavity. $B(\tilde{\omega})$ can be approximated as in Eq. (21), therefore $D(\tilde{\omega}) = 0$ equals solving

$$-\tilde{\omega}^2 + i\tilde{\omega}\Gamma_N + \frac{\tau_{in}\omega_r^2}{\tau_{tot}} = 0 \tag{23}$$

with ω_r being the same relaxation oscillation frequency of the Fabry-Perot case.

Equation (23) clearly evidences that the introduction of the external cavity with a frequency-independent reflection coefficient reduces the relaxation oscillation frequency (with respect to the FP case) of a factor $\sqrt{\tau_{in}/\tau_{tot}}$ but it does not change the damping rate. The result in Eq. (23) is consistent with [20], where the hybrid laser was approximated with an external cavity laser with frequency-independent r_{eff}. This is in general true when the parameter Γ_T (defined as $2\pi\Delta\nu_{FWHM}$ with $\Delta\nu_{FWHM}$ being the bandwidth of $r_{eff}(\omega)$) is much larger than Γ_N and ω_r. However, when the mirror bandwidth becomes narrower (i.e., when $\Gamma_T \approx 3 - 10$ GHz as in our case), the general Eq. (19) must be solved numerically since an analytical approximation becomes impossible. The same dependence of the relaxation oscillation on the ratio $\sqrt{\tau_{in}/\tau_{tot}}$ has been reported for the case of the Fano laser [19] and, similarly to [20], it was claimed that the reduction of the frequency of relaxation oscillations is beneficial in increasing the tolerance to the external optical feedback. However, the Fano laser in [19] is different from the laser structure studied here and in [20], because in [19], thanks to the photonic crystal microcavity, we have $1/\tau_{in} \gg \Gamma_T$: in this limit the Fano laser reaches the maximum possible damping factor of relaxation oscillations. In our case, we have that $1/\tau_{in}$ is only slightly larger than Γ_T; as shown in section 3, this still gives an important reduction of the damping factor even if not as high as the Fano laser case. Here, we also stress the fact that Eq. (19) allows to calculate not only the zeros of the characteristic equation due to carrier-photon interaction (i.e., laser relaxation oscillations), but also those due to interaction of the lasing mode with the other longitudinal cavity modes. Moreover, these results provide an explanation for the phenomena of mode-hopping, self-pulsing, and chaotic regimes observed in a laser with an external cavity, as well as in our case, in terms of four-wave mixing and phase-amplitude coupling provided by the alpha factor [17]. Additionally in this work we demonstrate that, in the hybrid laser case, the same characteristic equation can be also exploited to study the impact of the SiPh mirror on the laser relaxation oscillations and the effect of external optical feedback in the destabilization of continuous wave emission.

Optics EXPRESS

3. Dynamics of the solitary laser: instabilities and intensity modulation response

In order to obtain a general picture of the solitary laser ($r_{ext} = 0$) dynamics and confirm the results of SSA, we integrated Eqs. (2–5) by sweeping two external control parameters, represented by the bias current I and the detuning $\Delta\nu_s$ of the lasing mode frequency with respect to the effective reflectivity peak (by acting on the phase shift $\Delta\phi$ in the PS section) for a narrow reflectivity $|r_{eff}|^2$ of FWHM=3.1 GHz. In particular, we considered 30 values of bias current from 20 mA (just above the threshold current) to 250 mA and 30 values of detuning (corresponding to 30 values of $\Delta\phi$ between 0 and 2π). In all cases, we chose as initial condition the CW solution with the values of ω_s and N_s at the laser threshold obtained by solving Eqs. (10) and (11).

The map of the integrated Relative Intensity Noise (RIN) over a bandwidth of 25 GHz in Fig. 4 summarizes the outcome of these simulations. Here, the yellow area (with integrated RIN higher than −130 dBc/Hz) corresponds to a multimode regime where the considered CW solution has become unstable, while the blue area corresponds instead to a stable single mode regime (integrated RIN smaller than −160 dBc/Hz). The white dashed line is the border of instability obtained from the SSA. In order to explain the origin of instability in the yellow region of Fig. 4(a), we show the SSA results for a fixed value of $\Delta\nu_s = -2.7$ GHz and variable bias current (from 17 mA, slightly above threshold, to 250 mA), corresponding approximately to the vertical red solid line in panel (a). The trajectory of the zeros of the determinant $D(\tilde{\omega})$ given by Eq. (19) for this choice of parameters is reported in the complex plane in panel Fig. 4(b). Note that the zeros of the determinant of Eq. (19) are also poles of the modulation transfer function [26], therefore in the following we identify them equivalently with both names. We identify the poles in blue with the lasing mode relaxation oscillations (RO) while the poles in orange are associated with the Photon-Photon Resonance (PPR) resulting from the beating between the lasing mode and one adjacent cavity longitudinal mode [27]. Here, increasing values of bias current are associated with light to dark hues. The trajectory of the blue point, which eventually gives rise to instability, presents a null real part at threshold and grows in frequency for values of current above threshold. As the blue point frequency becomes resonant with the beating between the lasing mode and another longitudinal cavity mode (which is the solution of Eqs. (10) and (11)) for $\Delta\nu_s = -7$ GHz, $N_s = 7.5 \times 10^{17}$ cm^{-3}, and $m = -3$, resulting in a beating frequency at 4.3 GHz, indicated in Fig. 4(b) by the vertical black line), its trajectory crosses the real axis, leading to undamped oscillations and thus triggering the instability of the CW solution. This instability scenario is common to all parameter choices corresponding to the yellow region of Fig. 4(a). Note that the origin of the complex plane is always a solution of $D(\tilde{\omega}) = 0$ [17]. In Fig. 4(c) and 4(d), we also report the RIN spectra, obtained from dynamical simulations at fixed $\Delta\nu_s = -2.7$ GHz for two different bias currents. In particular, (c) corresponds to a stable case at $I = 50$ mA, highlighted by the green star in Fig. 4(a), and 4(d) correspond to a CW unstable regime at $I = 120$ mA, marked by the red star in (a). The frequency of the first peak in the RIN spectra of both Fig. 4(c) and 4(d) matches the frequency of relaxation oscillations obtained from the SSA represented by the green and red stars in 4(b) for the specific value of chosen bias current, as highlighted by the vertical green and red dashed lines in Fig. 4(c) and 4(d). Remarkably, we observe in Fig. 4(d) a self-pulsing regime in line with experimental results reported in [8,10], where a self-mode-locked regime is found by varying the current in the phase control section.

A comparison with the results of the laser intensity-modulation (IM) response allows to validate further the results of the SSA with those of dynamical simulations. As an example, in Fig. 5(a) we show the poles obtained from the SSA for effective reflectivity FWHM=6.2 GHz, $I = 104$ mA (corresponding to a typical target power of $P_{out} \approx 20$ mW [20]), and $\Delta\nu_s = -0.33$ GHz, i.e. close to the effective reflectivity peak. As previously mentioned, the two poles with the lowest damping rate are associated to RO and PPR. Note that, both poles at higher frequency values are associated to PPR with the nearest longitudinal modes, however, one of these is more damped and does not have a significant impact on the laser dynamics. According to the SSA, the laser is stable for this

Optics EXPRESS

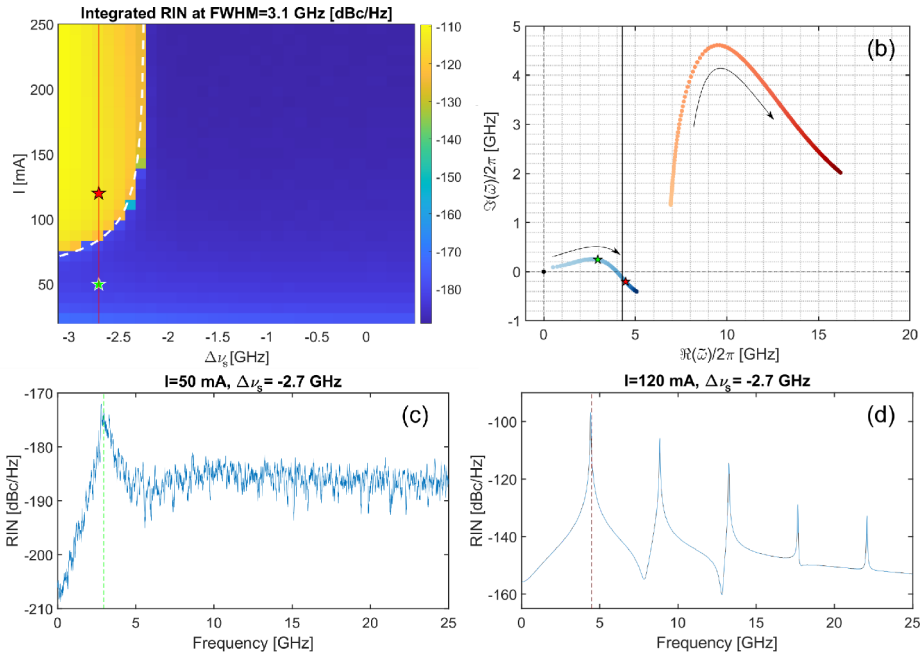

Fig. 4. (a) Map of the RIN integrated over a bandwidth of 25 GHz for different values of bias current and detuning of the lasing frequency and a reflectivity bandwidth FWHM=3.1 GHz. The white dashed line corresponds to the border of instability. (b) Plot of the trajectory of the zeros of the determinant $D(\tilde{\omega})$ for $\Delta\nu_s = -2.7$ GHz (corresponding to the vertical solid line in (a)) and bias current from 17 mA to 250 mA. For increasing values of current, the trajectory of each point evolves towards darker hues of the same color, following the arrow direction. The vertical black solid line indicates the beating of the lasing mode with another longitudinal cavity mode. (c-d) RIN spectra for $\Delta\nu_s = -2.7$ GHz and bias current $I = 50$ mA (c) and $I = 120$ mA (d), corresponding respectively to the green and red stars in (a). The RO poles highlighted in (b) with stars of the same color match the frequencies in dashed line in (c,d).

choice of parameters. This is confirmed in Fig. 5(b), where we show the intensity-modulation response, obtained through numerical integration of Eqs. (2–5). The vertical black dashed lines identify the frequency location of the two poles with the lowest damping rate in (a). Here, we can clearly relate the pole associated to the laser relaxation oscillations with the first peak of the IM response and the pole associated to PPR with the second high-frequency peak. Finally, in Fig. 5(c), we compare the IM response of the laser for different reflectivity FWHMs (matching those of Fig. 2) with the FP case defined in Subsection 2.2 and described by Eq. (22). All curves have been obtained for $\Delta\nu_s = -0.33$ GHz and $I = 104$ mA. Figure 5(c) shows that for the same value of detuning of the lasing frequency, relaxation oscillations exhibit a shift towards lower frequency and an increase of their damping. The shift of the relaxation oscillation frequency is as expected by the increase of the external cavity effective length (see Eq. (23)) and it is in line with what predicted in [19]. The increase of the damping factor (that we ascribe to a sort of filter of the relaxation oscillations through the narrow band mirror) is similar to what was theoretically predicted for the Fano laser in [28], even if, due to the micro-cavity in [28], smaller Q than in the present case are needed for a significant reduction of the damping. While the relevance of RO becomes lower with the introduction of a frequency-selective reflectivity, an additional pole related to mode competition emerges (second peak in Fig. 5(c)). As expected, the role of PPR becomes more relevant to the laser dynamics for larger reflectivity bandwidths. It is

Optics EXPRESS

worth mentioning that this trend is confirmed also when a FWHM limit value of sub-GHz [13] is considered in the analysis.

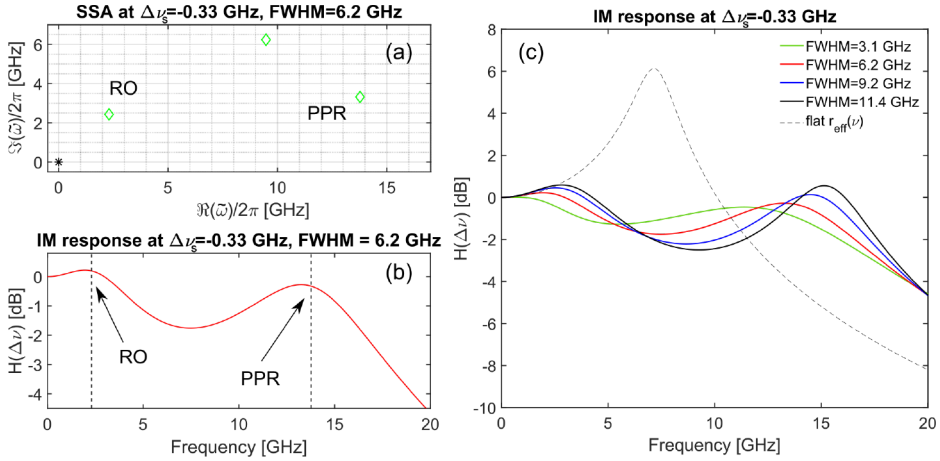

Fig. 5. (a) Plot of the poles of SSA for effective reflectivity FWHM=6.2 GHz, $\Delta\nu_s = -0.33$ GHz and $I = 104$ mA. The two poles with lower damping represent relaxation oscillations (RO) and photon-photon resonance (PPR). (b) Intensity-modulation response obtained through dynamical simulations. The black dashed lines highlight the value in frequency of the two poles in (a). (c) IM response at the same $I = 104$ mA and $\Delta\nu_s = -0.33$ GHz for different values of refectivity FWHM.The black dashed line is the FP case with $\alpha = 0$ [26].

In order to better understand the role of the narrow band mirror and the impact of the α-parameter on the damping of relaxation oscillations, we show in Fig. 6 the trajectory of the RO pole (in blue hues) as a function of the bias current for $\alpha = 0$ and $\alpha = 3$ and we compare these trajectory with those obtained by solving Eq. (22) and Eq. (23) respectively for the FP case (black dashed line) or for the external cavity with a flat mirror (violet dotted line). In particular, Fig. 6(a) is obtained for a value of detuning $\Delta\nu_s = 0$ GHz and Fig. 6(b) is plotted for $\Delta\nu_s = -1$ GHz. The red circle in each trajectory highlights the pole location for $I = 104$ mA.

As indicated in Fig. 6(a), the two blue trajectories for $\alpha = 0, 3$ overlap for $\Delta\nu_s = 0$ GHz, as expected, since the effect of the α factor is minimal on the reflectivity peak. The RO frequency is decreased by the introduction of the external cavity, and diminished further when a frequency-selective reflectivity is considered. As indicated in Eqs. (22–23), the damping rate remains the same for the two cases with flat reflectivity, while the introduction of a narrow-bandwidth reflectivity significantly increases the damping of relaxation oscillations. When we detune the lasing mode from the reflectivity peak, we observe a different damping factor in case of $\alpha = 0$ and $\alpha = 3$. For $\alpha = 3$ any carrier modulation induced by noise turns into a modulation of the lasing frequency which itself turns in an additional intensity modulation via the frequency-dependent reflectivity of the mirror. This motivates the reduction of the damping factor with respect to the case $\alpha = 0$. On the other hand, this effect is negligible in Fig. 6(a) because frequency modulations of the lasing mode cannot turn into intensity modulations due to the rather frequency-independent reflectivity around the peak.

Optics EXPRESS

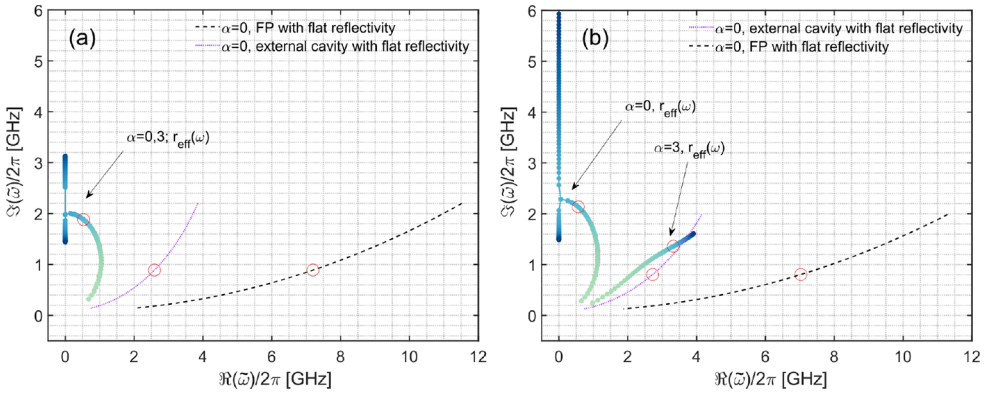

Fig. 6. (a) Plot of the RO pole trajectories (in blue hues) as functions of the bias current I, obtained from the SSA for effective reflectivity FWHM=3.1 GHz and (a) $\Delta\nu_s = 0$ GHz, (b) $\Delta\nu_s = -1$ GHz. The red circle on each trajectory highlights the pole location at $I = 104$ mA. In both (a,b) we show the (blue) trajectories for $\alpha = 0$ and $\alpha = 3$. We also plotted, in black dashed line, the trajectory of the RO pole in the case of a single-mode laser with flat reflectivity in frequency and, in violet dotted line, the trajectory of the RO pole in case of a single-mode laser with an external cavity and flat reflectivity.

4. Tolerance to external optical feedback

The aim of this section is discussing the impact of the narrow band mirror in improving the tolerance of the laser to unwanted external optical feedback. The improvement of the critical feedback level by the insertion of an external cavity mirror has already been studied in [19,20] and attributed to the reduction of the RO frequency as in Eq. (23); here, we focus on the impact of the reflector bandwidth. We performed a systematic study of the solitary laser for different reflectivity bandwidth and fixed effective length L_{eff}, computed as indicated in Eq. (7). In practice, this can be achieved by including an additional piece of waveguide of variable length in the SiPh circuit before the splitter in Fig. 1. This allows to isolate the role of the effective reflectivity bandwidth in the laser stability. This choice makes the results of the present paper complementary to those in [20].

In Fig. 7, we show the results of dynamical simulations of Eqs. (2–5), for hybrid lasers with $R_{ext} = r_{ext}^2 = 0$, through the maps of integrated RIN for FWHM=3.1 (a), 6.2 (b), 9.2 (c), 11.4 (d) GHz. The chosen fixed value of effective reflectivity $L_{eff} = 1.295$ cm is the same considered for simulations in Fig. 4. Note that, in order to make the maps in Fig. 7(a-d) comparable on the horizontal axis we extended the range of detuning beyond the values achievable from the oscillation condition, resulting in the presence of white regions (notably in 7(a) and also partially in 7(b-d)). The low RIN (blue) areas that are encompassed by the border of instability in Fig. 7(b-d) are still regions of CW operation where however the lasing frequency has jumped to that of another mode with a carrier density above its value at threshold (mode hopping). We can also clearly notice that in all four cases the detuning range on the x-axis is asymmetric with respect to $\Delta\nu_s = 0$ GHz due to the asymmetry of the lasing mode solutions of Eq. (11) for $\alpha \neq 0$. For all values of bias current in Fig. 7 we can find a range in $\Delta\nu_s$ for which the CW lasing emission is always stable. The values of this range are reported in Fig. 7(e), showing a larger stable region for the middle point corresponding to FWHM=6.2 GHz. Except for Fig. 7(a), which has been already analyzed in detail, the CW instability in 7(b-d) occurs for positive $\Delta\nu_s$, implying that most of the stable region lies in a negative range of detuning. A justification of this evidence can be found in the negative feedback (detuned loading) effect, a mechanism exploited also in the realization of narrow linewidth hybrid lasers [9]. As a result of this effect, negative values of

Optics EXPRESS

detuning result more stable since any instantaneous positive frequency fluctuation would here imply an increase in reflectivity and photon density and therefore a decrease in carrier density, which, in turn, would cause the frequency to decrease due to phase-amplitude coupling mediated by α, bringing the detuning back to its original value. For a similar reasoning, perturbations of a CW solution with $\Delta\nu_s>0$, are less likely to keep the laser stable due to the triggering of an opposite (positive) feedback loop. Differently from Fig. 7(a), where we already proved that instability occurs due to RO becoming undamped (when resonant with the beating between longitudinal cavity modes) the main cause of instability for larger FWHMs is closely related to PPR becoming more relevant with the increase of the mirror bandwidth.

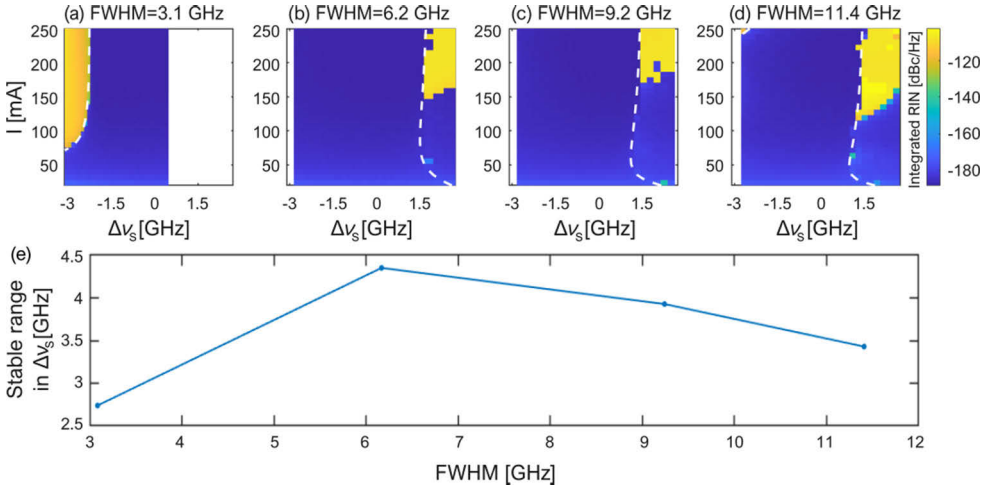

Fig. 7. Maps of the RIN integrated over a bandwidth of 25 GHz for different values of bias current and detuning of the lasing frequency. Figs (a,b,c,d) correspond to the different values of effective reflectivity FWHM (3.1 GHz, 6.2 GHz, 9.2 GHz, 11.4 GHz, respectively). Simulations have been run for lasers with the same L_{eff} (i.e. including an additional piece of waveguide of 5.64 mm, 7.5 mm and 8.2 mm for cases (b-d) respectively). The white dashed line corresponds to the border of instability predicted from the SSA.

In Section 2 we have demonstrated that the hybrid laser has two resonances: RO and PPR. We expect that the less damped resonance (between the two) will be destabilized by the external feedback and will lead to undamped oscillations. Note that the standard Lang-Kobayashi approach adopted in [20] does not consider PPR and therefore cannot capture all possible causes of instability in hybrid lasers. Furthermore, the absence of a frequency dependence in the effective reflectivity in the Lang-Kobayashi model implies no dependence of the pole frequency and damping factor on the detuning.

To evaluate the damping of RO and PPR at different detuning and different effective reflectivity FWHM in the stable range, we show in Fig. 8(a) and 8(b) the poles obtained by the SSA for FWHM=3.1 GHz (dots) and 6.2 GHz (squares) for I=104 mA. We do not report the poles for FWHM=9.2, 11.4 GHz because their dependence on the detuning is fairly similar to the case of FWHM=6.2 GHz. Light blue curves relate to the RO pole, whereas the orange curves relate to PPR. As evident in Fig. 8(b) for FWHM=6.2 GHz, the orange pole is the least damped (and will eventually give rise to instability for positive detunings beyond the stable range). On the other hand, PPR has no relevant impact on stability for FWHM=3.1 GHz.

In Fig. 8(c), we report the imaginary part of the pole with the minimum damping factor (between the RO and PPR) as a function of the laser detuning for all FWHMs. Except for FHWM=3.1 GHz, the poles with minimum damping factor are those of PPR, which is the

Optics EXPRESS

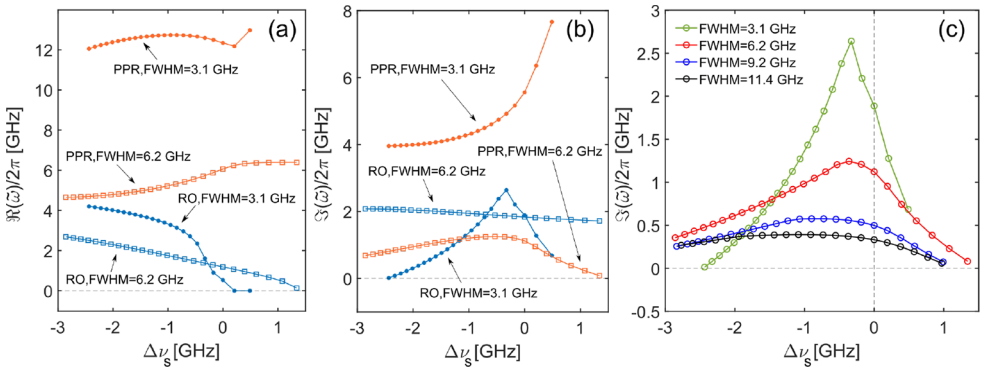

Fig. 8. Curves of real (a) and imaginary (b) part of the poles from SSA contributing to the laser dynamics, as a function of the lasing mode detuning for FWHM=3.1 GHz (dots) and FWHM=6.2 GHz (squares) and I = 104 mA. The light blue curves are associated to relaxation oscillations while the orange curves are associated to photon-photon resonance. (c) Plot of the imaginary part of the pole with the minimum damping factor for all FWHMs (same color code as in Fig. 2).

process that gives rise to instability when we add external optical feedback. The peak of all curves, corresponding to a condition of higher stability for the laser, always occurs for negative detunings close to $\Delta\nu_s$ = 0 GHz, which can be justified by the earlier described detuned loading effect. Figure 8(c) also shows that the broader is the reflectivity bandwidth, the lower is the associated minimum damping in the stable laser domain, which intrinsically implies less tolerance to feedback induced perturbations. On the other hand, Fig. 7(e) also shows that the range of stability for any bias current is larger for FWHM=6.2 GHz, mainly due to the fact that the overall available detuning range is more restricted for FWHM=3.1 GHz, which would suggest a potential resilience to unwanted optical back reflections for a larger range of detuning. Further, for large detuning values ($\Delta\nu_s \approx -2$ GHz), we can argue (also from Fig. 8(c)) that this reflectivity bandwidth potentially shows more stability against external perturbations.

4.1. Calculation of the critical feedback level

We now address how the introduction of optical feedback affects the laser stability, allowing us to identify the best parametric region for design. We consider an external cavity length L_{ext} =0.5 cm, which emulates a typical distance from which we expect spurious back reflections from the SiPh circuit.

In Fig. 9, we report the trajectory of the SSA poles for increasing values of external reflectivity R_{ext} (from −60 dB to ≈ −10 dB), effective reflectivity FWHM=3.1 GHz, I = 104 mA and two different values of detuning i.e. $\Delta\nu_s = -1$ GHz (Fig. 9(a)) and $\Delta\nu_s = -0.22$ GHz (Fig. 9(b)). Note that any result obtained for R_{ext}>−10 dB would potentially be inconclusive in the context of addressing the tolerance of the hybrid laser to spurious back reflections, since it considers a laser with external optical feedback reflection coefficient much higher than the effective reflection coefficient of the SiPh mirror.

As evident from Fig. 9(a) and 9(b), the poles associated to the modes of the external cavity introduced by the external optical feedback (i.e., light to dark green poles in Fig. 9(a) and 9(b)) are initially highly damped ($\Im(\tilde{\omega})/2\pi$>20 GHz) and move towards lower values of damping for increasing values of R_{ext}, therefore becoming relevant in the laser dynamics, since their damping becomes comparable with the damping of the RO and PPR poles, which in turn also move towards lower $\Im(\tilde{\omega})$. Instability generates as soon as one of the plotted poles crosses the real axis, which occurs at the critical feedback level of $R_{ext,crit} \approx -18$ dB in Fig. 9(a) for $\Delta\nu_s = -1$

Optics EXPRESS

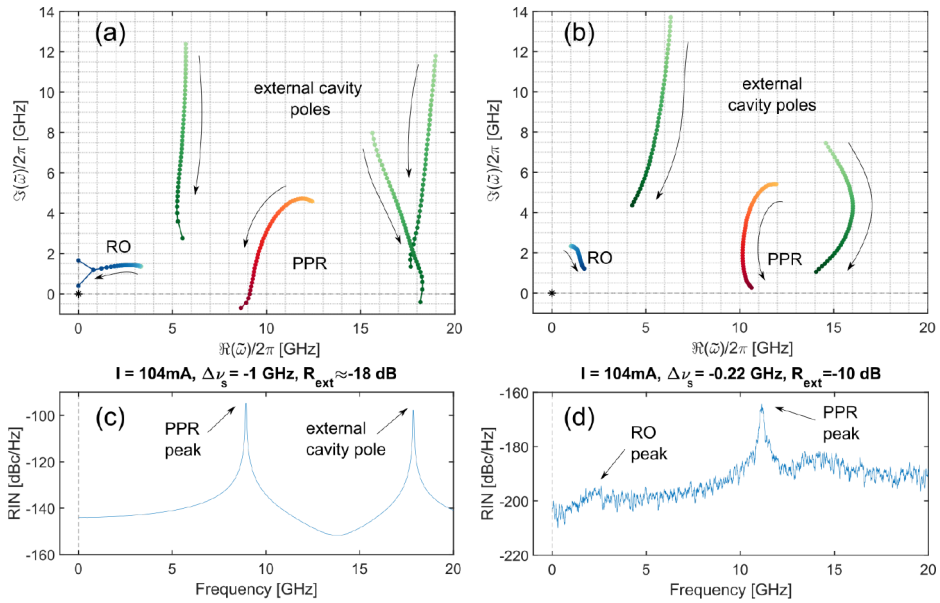

Fig. 9. (a-b) Trajectory of the SSA poles for increasing values of R_{ext} (from −60 dB to ≈ −10 dB, i.e. from light to dark hues of the same color). Arrows indicate the direction for increasing R_{ext}. Results are for effective reflectivity FWHM=3.1 GHz, L_{ext} = 0.5 cm, I = 104 mA, and detuning of the solitary lasing mode (a) $\Delta\nu_s = -1$ GHz and (b) $\Delta\nu_s = -0.22$ GHz. Following the same color coding as Fig. 4(b), the RO pole is in blue and the PPR pole is in orange. The additional poles due to the external feedback (i.e., the external cavity modes) are displayed in green. RIN spectra (c) near the critical feedback level for $\Delta\nu_s = -1$ GHz at $R_{ext} = -18$ dB and (d) for $\Delta\nu_s = -0.22$ GHz and $R_{ext} = -10$ dB.

GHz. The critical feedback level $R_{ext,crit}$ is defined as the as the value of R_{ext} where the CW emission becomes unstable. In this case, instability is triggered by the PPR which first becomes undamped. The RIN spectrum reported in Fig. 9(c) for $R_{ext} \approx -18$ dB displays two main peaks, corresponding to the frequency location of the PPR pole and the external cavity pole that have crossed the $\Im(\tilde{\omega}) = 0$ axis.

When the detuning $\Delta\nu_s$ is further reduced, we enter in the high-damping region reported in Fig. 8(c) where we expect a higher critical feedback level. In fact for $\Delta\nu_s = -0.22$ GHz we show in Fig. 9(b) that the laser remains stable up to $R_{ext,crit} = -10$ dB. This result is also confirmed by the RIN spectrum in Fig. 9(d), where a peak associated to the PPR resonance starts to emerge but still displays very low values. This result anticipates the existence of an ultra-stable detuning region close to the effective reflectivity peak where the laser is particularly resilient to optical feedback up to an external reflectivity of $R_{ext} = -10$ dB.

This is what is shown in Fig. 10(a), where we report, for each effective reflectivity FWHM indicated in Fig. 2, the critical feedback level $R_{ext,crit}$. The results have been obtained through systematic simulations for a scan of the detuning values for which the solitary laser solution is stable at I = 104 mA. The shaded regions highlight the detuning range of ultra-stability for each chosen reflectivity FWHM. We can notice that the laser appears to be ultra-stable also in a positive detuning region. However, we would like to point out that the detuning value reported in Fig. 10 always refers to the solitary laser CW emission for the sake of comparison between simulations performed with different values of external reflectivity. These nominal $\Delta\nu_s$ values may slightly differ from the actual lasing frequency, which can be modified as an effect of R_{ext}: in particular, in the observed ultra-stable cases with positive detuning, the CW emission has shifted

Optics EXPRESS

to negative lasing frequencies. From Fig. 10(a) we can also observe that the effective reflectivity FWHM=6.2 GHz exhibits, as expected, the largest ultra-stable range, which reflects some of the considerations made in relation to Fig. 7(e). On the other hand, for applications of the hybrid laser that require a feedback tolerance up to −20 dB, we note that the curve for FWHM=3.1 GHz allows for larger detuning in presence of spurious back-reflections. This is because, while the solitary laser poles are usually the ones here triggering the instability, the external cavity poles may still play a role in determining which of the solitary laser pole first crosses the real axis: in fact for FWHM=3.1 GHz, as already illustrated in Fig. 9(a), close to the ultra-stable region, the pole associated to PPR is closer to the external cavity poles and therefore more likely to play a relevant role in the laser dynamics. On the other hand, since the PPR pole is generally more damped than the RO pole for FWHM=3.1 GHz, the green curve displays a more stable range than the other mirror bandwidths.

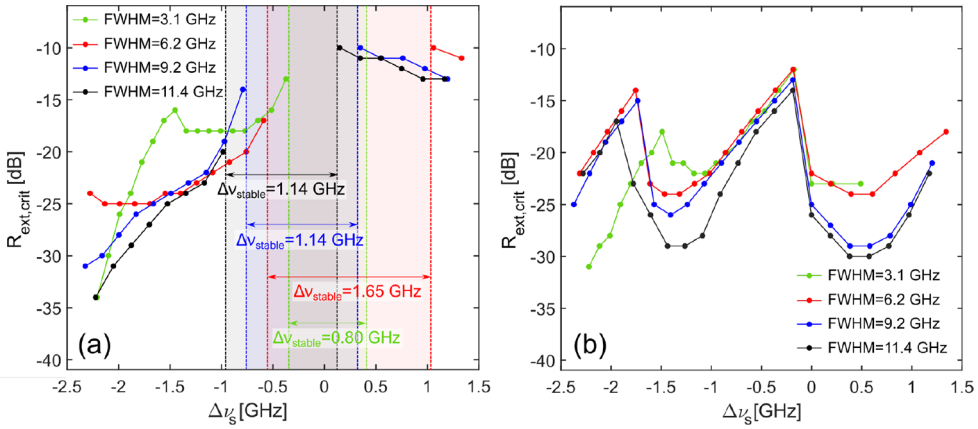

Fig. 10. Critical feedback level $R_{ext,crit}$ as a function of the laser detuning for the indicated effective reflectivity FWHM and for (a) L_{ext} =0.5 cm and (b) L_{ext} =5 cm. The shaded regions in (a) highlight the range of laser ultra-high stability with respect to the cavity external reflectivity for the effective reflectivity FWHM of the matching color.

In Fig. 10(b) we show similar curves of critical feedback level for L_{ext} = 5 cm. This would corresponds to a worse case in terms of back reflections with respect to the previous one (L_{ext} = 0.5 cm) since large external lengths tend to be associated to a larger laser instability [26]. When we increase the external length the number of poles associated to the external cavity increases as well and the pole trajectories become more complex, as shown in Fig. 11 for $\Delta\nu_s = -1.28$ GHz and $\Delta\nu_s = -0.18$ GHz. For detuning $\Delta\nu_s = -1.28$ GHz, the instability occurs at $R_{ext,crit} = -24$ dB (Fig. 11(a)), whereas for detuning $\Delta\nu_s = -0.18$ GHz we have $R_{ext,crit} = -12$ dB (Fig. 11(b)). The pole associated to this instability is a solitary laser pole related to PPR in case 11(a) and an external cavity pole in case 11(b). As expected, we can observe that, for very low values of damping, the separation between the external cavity poles that are closer to the real axis is compatible with the external cavity FSR.

As emerges from Fig. 10(b), while the laser ultra-stable region disappears, a region with $R_{ext,crit} > -15$ dB still remains for detuning around $\Delta\nu_s = 0$ GHz. Differently from the previous case, Fig. 10(b) shows the presence of two peaks of $R_{ext,crit}$ obtained for two different detunings. The peak closer to $\Delta\nu_s = 0$ GHz matches the condition of high damping reported in Fig. 8(c): here, as exemplified in Fig. 11(b), instability is usually associated to the external cavity poles, which is expected since the RO and PPR poles are very damped. The valley between the two peaks corresponds to a condition of detuning where the role of the solitary laser poles has become more relevant: here instability usually arises due to undamped RO in the case of reflectivity

Optics EXPRESS

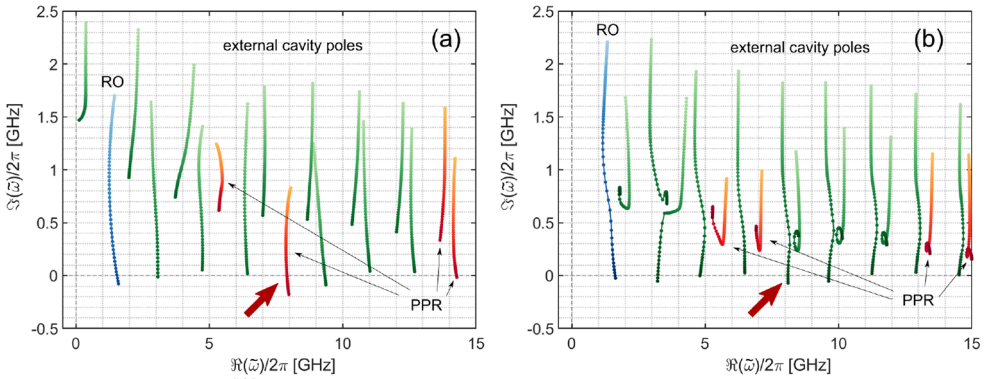

Fig. 11. Trajectory of the LSA poles for increasing values of R_{ext} (from −60 dB to ≈ −10 dB) for effective reflectivity FWHM=6.2 GHz, L_{ext} = 5 cm, I=104 mA, and detuning of the solitary lasing mode (a) $\Delta\nu_s = -1.28$ GHz and (b) $\Delta\nu_s = -0.18$ GHz. Instability occurs at (a) $R_{ext,crit} = -24$ dB (b) $R_{ext,crit} = -12$ dB. The color coding is the same as in Fig. 9. The red arrow highlights the pole giving rise to instability.

FWHM=3.1 GHz or undamped PPR for the other cases of FWHM or external cavity poles that become resonant with RO or PPR. We can also observe that in this valley, larger FWHMs exhibit a lower $R_{ext,crit}$, which is an effect of the lower damping for the solitary laser shown in Fig. 8(c). Finally, the peak developing for lower detunings occurs simply due to a favorable mode configuration of the hybrid laser in presence of feedback, where, up to the point indicated by $R_{ext,crit}$, other modes are particularly distant from the lasing one.

While the effective reflectivity FWHM=3.1 GHz shows a lower slope of $R_{ext,crit}$ as a function of $\Delta\nu_s$ in Fig. 10(a) and 10(b), the FWHM=6.2 GHz has the largest ultra-stable range in 10(a). This allows to identify these two values of reflectivity bandwidths as the optimal ones for a feedback-resilient hybrid laser design; additionally they also show a comparable CW stability in the absence of feedback (as illustrated in Fig. 8(c)). Overall, a larger range of stability in $\Delta\nu_s$ (with comparable damping) may in practice be preferrable, especially when a limited control of the detuning of the lasing mode is available. Further, through our study we have been able to identify the best detuning range for laser operation. Finally, in the very interesting perspective of using quantum dots based active material in the new generation of SiPh transmitters [29], we performed a set of dynamical simulations for α=0 (not reported here) that confirms the increased resilience to optical feedback of small α devices, as expected using much more simplified models based on the Lang-Kobayashi approach [20].

5. Conclusions

We studied the CW stability of III-V/SiN external cavity lasers with dispersive narrow band mirrors. As an example we have analyzed a structure consisting of a RSOA and an external cavity mirror made of two coupled rings; we have varied the ring coupling coefficients to design mirrors with different bandwidth of the reflection coefficients. We have presented a model that can be employed to analyze the stability of these lasers by varing the lasing wavelength and/or the bias current, also in presence of external optical feedback. With respect to the standard Lang-Kobayashi approach, our model allows to take into account the amplitude and frequency dispersion of the mirror, the other laser cavity longitudinal modes, and the detuning of the lasing wavelength with respect to the peak of the reflection coefficient of the mirror. We demonstrate that mirrors with narrow bandwidths are effective in suppressing the laser relaxation oscillations for a range of detuning of lasing wavelength and for low alpha-parameters. However, we also

Optics EXPRESS

demonstrate that a second resonance due to PPR cannot be neglected and it can be the trigger of laser instability in presence of external back reflection. We have determined, for equal effective lengths of the laser cavity, the best parametric region for the design of a hybrid laser that is tolerant to spurious back reflections and we have identified in this region the presence of a potentially ultra-stable regime for a specific detuning range. The obtained results have potential applications in the design of isolator-free lasers and/or can be used to interpret or guide the dynamic characterization of these laser structures.

Acknowledgments. This work is supported under a CISCO Sponsored Research Agreement. The authors acknowledge Dr. Fabrizio Forghieri (Cisco Photonics, Vimercate, Italy) for coordinating the project.

Disclosures. The authors declare that there are no conflicts of interest related to this article.

Data Availability. Data underlying the results presented in this paper are not publicly available at this time but may be obtained from the authors upon reasonable request.

Supplemental document. See Supplement 1 for supporting content.

References

1. C. G. Littlejohns, D. J. Rowe, H. Du, K. Li, W. Zhang, W. Cao, T. Dominguez Bucio, X. Yan, M. Banakar, D. Tran, S. Liu, F. Meng, B. Chen, Y. Qi, X. Chen, M. Nedeljkovic, L. Mastronardi, R. Maharjan, S. Bohora, A. Dhakal, I. Crowe, A. Khurana, K. C. Balram, L. Zagaglia, F. Floris, P. O'Brien, E. Di Gaetano, H. M. Chong, F. Y. Gardes, D. J. Thomson, G. Z. Mashanovich, M. Sorel, and G. T. Reed, "Cornerstone's silicon photonics rapid prototyping platforms: Current status and future outlook," Appl. Sci. **10**(22), 8201 (2020).
2. W. Bogaerts, S. K. Selvaraja, H. Yu, T. Spuessens, P. Mechet, S. Stankovic, S. Keyvaninia, J. V. Campenhout, P. Absil, G. Roelkens, D. V. Thourhout, and R. Baets, "A silicon photonics platform with heterogeneous iii-v integration," in *Advanced Photonics*, (Optical Society of America, 2011), p. IWC2.
3. S. Y. Siew, B. Li, F. Gao, H. Y. Zheng, W. Zhang, P. Guo, S. W. Xie, A. Song, B. Dong, L. W. Luo, C. Li, X. Luo, and G.-Q. Lo, "Review of silicon photonics technology and platform development," J. Lightwave Technol. **39**(13), 4374–4389 (2021).
4. S. Lin, X. Zheng, J. Yao, S. S. Djordjevic, J. E. Cunningham, J.-H. Lee, I. Shubin, Y. Luo, J. Bovington, D. Y. Lee, H. D. Thacker, K. Raj, and A. V. Krishnamoorthy, "Efficient, tunable flip-chip-integrated iii-v/si hybrid external-cavity laser array," Opt. Express **24**(19), 21454–21462 (2016).
5. H. Park, A. W. Fang, S. Kodama, and J. E. Bowers, "Hybrid silicon evanescent laser fabricated with a silicon waveguide and iii-v offset quantum wells," Opt. Express **13**(23), 9460–9464 (2005).
6. E. N. T. Komljenovic, S. Srinivasan, M. Davenport, G. Fish, and J. E. Bowers, "Widely tunable narrow-linewidth monolithically integrated external-cavity semiconductor lasers," IEEE J. Sel. Top. Quantum Electron. **21**(6), 214–222 (2015).
7. Y. Fan, R. E. M. Lammerink, J. Mak, R. M. Oldenbeuving, P. J. M. van der Slot, and K.-J. Boller, "Spectral linewidth analysis of semiconductor hybrid lasers with feedback from an external waveguide resonator circuit," Opt. Express **25**(26), 32767–32782 (2017).
8. D. Huang, M. A. Tran, J. Guo, J. Peters, T. Komljenovic, A. Malik, P. A. Morton, and J. E. Bowers, "High-power sub-khz linewidth lasers fully integrated on silicon," Optica **6**(6), 745–752 (2019).
9. M. A. Tran, D. Huang, and J. E. Bowers, "Tutorial on narrow linewidth tunable semiconductor lasers using si/iii-v heterogeneous integration," APL Photonics **4**(11), 111101 (2019).
10. J. Mak, A. van Rees, Y. Fan, E. J. Klein, D. Geskus, P. J. M. van der Slot, and K.-J. Boller, "Linewidth narrowing via low-loss dielectric waveguide feedback circuits in hybrid integrated frequency comb lasers," Opt. Express **27**(9), 13307–13318 (2019).
11. Y. Fan, A. van Rees, P. J. M. van der Slot, J. Mak, R. M. Oldenbeuving, M. Hoekman, D. Geskus, C. G. H. Roeloffzen, and K.-J. Boller, "Hybrid integrated inp-si3n4 diode laser with a 40-hz intrinsic linewidth," Opt. Express **28**(15), 21713–21728 (2020).
12. C. Xiang, W. Jin, J. Guo, C. Williams, A. M. Netherton, L. Chang, P. A. Morton, and J. E. Bowers, "Effects of nonlinear loss in high-q si ring resonators for narrow-linewidth iii-v/si heterogeneously integrated tunable lasers," Opt. Express **28**(14), 19926–19936 (2020).
13. C. Xiang, P. A. Morton, J. Khurgin, C. Morton, and J. E. Bowers, "Widely tunable si3n4 triple-ring and quad-ring resonator laser reflectors and filters," in *2018 IEEE 15th International Conference on Group IV Photonics (GFP)*, (2018), pp. 1–2.
14. G. Morthier, "Feedback sensitivity of dbr-type laser diodes," IEEE Photonics J. **13**(4), 1–5 (2021).
15. Y. Matsui, R. Schatz, D. Che, F. Khan, M. Kwakernaak, and T. Sudo, "Low-chirp isolator-free 65-ghz-bandwidth directly modulated lasers," Nat. Photonics **15**(1), 59–63 (2021).
16. C. Xiang, P. A. Morton, and J. E. Bowers, "Ultra-narrow linewidth laser based on a semiconductor gain chip and extended si3n4 bragg grating," Opt. Lett. **44**(15), 3825–3828 (2019).
17. E. Detoma, B. Tromborg, and I. Montrosset, "The complex way to laser diode spectra: example of an external cavity laser strong optical feedback," IEEE J. Quantum Electron. **41**(2), 171–182 (2005).

Optics EXPRESS

18. Z. Zhang, D. Jung, J. C. Norman, W. W. Chow, and J. E. Bowers, "Linewidth enhancement factor in inas/gaas quantum dot lasers and its implication in isolator-free and narrow linewidth applications," IEEE J. Sel. Top. Quantum Electron. **25**(6), 1–9 (2019).
19. T. S. Rasmussen, Y. Yu, and J. Mork, "Suppression of coherence collapse in semiconductor fano lasers," Phys. Rev. Lett. **123**(23), 233904 (2019).
20. L. Columbo, J. Bovington, S. Romero-Garcia, D. F. Siriani, and M. Gioannini, "Efficient and optical feedback tolerant hybrid laser design for silicon photonics applications," IEEE J. Sel. Top. Quantum Electron. **26**(2), 1–10 (2020).
21. C. Schelte, D. Hessel, J. Javaloyes, and S. V. Gurevich, "Dispersive instabilities in passively mode-locked integrated external-cavity surface-emitting lasers," Phys. Rev. Appl. **13**(5), 054050 (2020).
22. L. Chrostowski and M. Hochberg, *Silicon Photonics Design: From Devices to Systems* (Cambridge University Press, 2015).
23. B. Tromborg, H. Olesen, X. Pan, and S. Saito, "Transmission line description of optical feedback and injection locking for fabry-perot and dfb lasers," IEEE J. Quantum Electron. **23**(11), 1875–1889 (1987).
24. T. S. Rasmussen, Y. Yu, and J. Mork, "Modes, stability, and small-signal response of photonic crystal fano lasers," Opt. Express **26**(13), 16365–16376 (2018).
25. B. Tromborg, J. Mørk, and V. Velichansky, "On mode coupling and low-frequency fluctuations in external-cavity laser diodes," Quantum Semiclassical Opt. **9**(5), 831–851 (1997).
26. L. A. Coldren and S. W. Corzine, *Semiconductor and Photonic Integrated Circuits* (John Wiley & Sons, Ltd, 1995).
27. P. Bardella and I. Montrosset, "A new design procedure for dbr lasers exploiting the photon–photon resonance to achieve extended modulation bandwidth," IEEE J. Sel. Top. Quantum Electron. **19**(4), 1502408 (2013).
28. J. Mork, Y. Yu, T. S. Rasmussen, E. Semenova, and K. Yvind, "Semiconductor fano lasers," IEEE J. Sel. Top. Quantum Electron. **25**(6), 1–14 (2019).
29. F. Grillot, J. C. Norman, J. Duan, Z. Zhang, B. Dong, H. Huang, W. W. Chow, and J. E. Bowers, "Physics and applications of quantum dot lasers for silicon photonics," Nanophotonics **9**(6), 1271–1286 (2020).